Evolution of the precipitate composition during annealing of vanadium micro-alloyed steels by in-situ SANS

Ioannidou, Chrysoula; Navarro-López, Alfonso; Rijkenberg, Arjan; Dalgliesh, Robert M.; Koelling, Sebastian; Pappas, Catherine; Sietsma, Jilt; van Well, Ad A.; Offerman, S.E.

DOI
10.1016/j.actamat.2020.09.083

Publication date
2020

Document Version
Final published version

Published in
Acta Materialia

Acta Materialia 201 (2020) 217–230

Contents lists available at ScienceDirect

Acta Materialia

journal homepage: www.elsevier.com/locate/actamat

Evolution of the precipitate composition during annealing of vanadium micro-alloyed steels by in-situ SANS

Chrysoula Ioannidou[a,*], Alfonso Navarro-López[a], Arjan Rijkenberg[b], Robert M. Dalgliesh[c], Sebastian Koelling[d,1], Catherine Pappas[e], Jilt Sietsma[a], Ad A. van Well[e], S. Erik Offerman[a]

[a] Department of Materials Science and Engineering, Delft University of Technology, Mekelweg 2, 2628 CD Delft, The Netherlands
[b] Tata Steel, 1970 CA IJmuiden, The Netherlands
[c] STFC, ISIS, Rutherford Appleton Laboratory, Chilton, Oxfordshire, OX11 0QX, United Kingdom
[d] Department of Applied Physics, Eindhoven University of Technology, PO Box 513, 5600 MB Eindhoven, The Netherlands
[e] Department of Radiation Science and Technology, Faculty of Applied Sciences, Delft University of Technology, Mekelweg 15, 2629 JB Delft, The Netherlands

ARTICLE INFO

Article history:
Received 29 May 2020
Revised 15 September 2020
Accepted 26 September 2020
Available online 1 October 2020

Keywords:
vanadium carbides
chemical composition evolution
in-situ Small-Angle Neutron Scattering
Atom Probe Tomography
vanadium micro-alloyed steels

ABSTRACT

In-situ Small-Angle Neutron Scattering (SANS) is used to determine the time evolution of the chemical composition of precipitates at 650 °C and 700 °C in three micro-alloyed steels with different vanadium (V) and carbon (C) concentrations. Precipitates with a distribution of substoichiometric carbon-to-metal ratios are measured in all steels. The precipitates are initially metastable with a high iron (Fe) content, which is gradually being substituted by vanadium during isothermal annealing. Eventually a plateau in the composition of the precipitate phase is reached. Faster changes in the precipitate chemical composition are observed at the higher temperature in all steels because of the faster vanadium diffusion at 700 °C. At both temperatures, the addition of more vanadium and more carbon to the steel has an accelerating effect on the evolution of the precipitate composition as a result of a higher driving force for precipitation. Addition of vanadium to the nominal composition of the steel leads to more vanadium rich precipitates, with less iron and a smaller carbon-to-metal ratio. Atom Probe Tomography (APT) shows the presence of precipitates with a distribution of carbon-to-metal ratios, ranging from 0.75 to 1, after 10 h of annealing at 650 °C or 700 °C in all steels. These experimental results are coupled to ThermoCalc equilibrium calculations and literature findings to support the Small-Angle Neutron Scattering results.

1. Introduction

High-performance steels with high strength, ductility and stretch flange-ability are required nowadays in lightweight automotive parts for low fuel consumption, reduced CO_2 emission and little use of raw materials [1]. Nano-steels have attracted both industrial and technological interest due to their high potential to meet these demands [2-8]. Their outstanding mechanical properties arise from the combination of a ferritic matrix with nano-sized precipitates. The ferritic phase offers high ductility while a substantial degree of strengthening originates from the presence of precipitates. Vanadium carbide precipitates are well known for precipitation strengthening [5,9], therefore, much research has been conducted on their effect on the mechanical properties of steels with various compositions that are processed under different conditions [9-13].

The chemical composition of the precipitates is a key factor for the precipitation strengthening since it drives the precipitation kinetics through the chemical driving force and the precipitate-matrix lattice misfit which control the precipitates nucleation and growth [14-16], eventually affecting the precipitate size distribution and the resulting mechanical properties. A high iron concentration in the vanadium carbides at the early stage of precipitation can reduce the lattice misfit and the strain energy between the precipitate and the matrix and, therefore, reduce the activation energy for the nucleation of the precipitate [15,16]. In turn, this leads to a high number density of precipitates, which is beneficial for the strength of the steel. In addition, the fraction of vanadium and the carbon to vanadium ratio in the precipitates can be important for the strengthening since it can affect the shear modulus of the precipitates [17-19] and eventually the modulus hardening which is caused by a modulus difference between the precipitates and the matrix (even though it is weak compared with other mechanisms

* Corresponding author.
E-mail address: c.ioannidou@tudelft.nl (C. Ioannidou).
[1] Current address: Department of Engineering Physics, École Polytechnique, Montréal, Québec H3C 3A7, Canada.

https://doi.org/10.1016/j.actamat.2020.09.083

of precipitation strengthening) [20]. It is reported in the literature that vanadium carbides with different carbon-to-metal atomic ratio show different mechanical properties such as Young's modulus, shear modulus and hardness [17-19], because of the different atomic configuration in the precipitates [17]. The abovementioned material properties are promoted for precipitates with a composition closer to stoichiometry [17]. The binding energy between the vanadium and carbon atoms in nano-sized precipitates can be influenced by the ferrite matrix. The presence of vacancies in the precipitates can reduce their interfacial energy and increase their stability [14]. Knowledge on the chemical composition evolution of precipitates during processing can contribute to an improved commercial steel design, optimized manufacturing and optimum use of critical raw materials.

The vanadium carbide precipitates have a Baker Nutting orientation relationship with the ferrite matrix [5] and they form in different shapes (spherical, disk-like, ellipsoidal, rod-like, needle-like or cuboid) with their shape and composition being dependent on steel composition and thermo-mechanical treatment conditions. Based on literature data, the vanadium carbides in low-carbon steels have a NaCl-type crystal structure with chemical formula: VC [21], V_4C_3 [5,21], $VC_{0.9}$ [13], $VC_{0.81}$ [22] or $VC_{0.75-0.92}$ [23]. In medium-carbon vanadium micro-alloyed steels the precipitates can be either NaCl-type of composition $VC_{0.72-0.9}$, depending on the processing temperature [24], V_6C_5 monoclinic or hexagonal [25] or V_4C_3 trigonal [25].

Earlier studies on the chemical composition of precipitates by means of APT in vanadium micro-alloyed steels [26] but also in titanium micro-alloyed steels [27,28] and in nickel-aluminium-molybdenum steels confirm the presence of iron in the precipitates [29]. APT measurements show gradual changes in the precipitate chemical composition during isothermal annealing at 650°C [26], while the precipitate chemical composition evolution is strongly correlated to the precipitate size [26,34]. In ref. [26], the smaller vanadium carbides are found to be iron-rich and the larger precipitates in the later stages of annealing are rich in iron only near the matrix/precipitate interface. Possibly a small fraction of iron is present in the core of the larger precipitates but they mainly consist of vanadium and carbon. Similar findings are presented in ref. [27] and in ref. [29], where it is stated that the iron content decreases across the particle interface from the surface to the core but still a considerable fraction of iron is measured in the precipitate core.

Transmission Electron Microscopy (TEM) and other TEM-based and spectroscopy techniques are often being used for precipitate characterisation [4,10-13,21-22,24-42]. These techniques are performed at room temperature, in a limited number of treated samples sampling a small area. Consequently, the sample preparation and treatment is time-consuming when aiming for results with good statistics. If the precipitate composition evolution needs to be measured, the characterisation procedure requires time and preparation [30]. In addition, quantitative analysis of the precipitates' chemical composition is challenging in the case of APT measurements because of the technique's limitations. By APT, the stoichiometry of the precipitates cannot be accurately quantified due to the directional walk effect that lowers the accuracy in the measured carbon concentration [43]. Moreover, the local magnification effect, caused by the field evaporation potential being different between the iron matrix and the precipitates, deteriorates the spatial resolution in the vicinity of small clusters and makes it difficult to quantify the iron content in the precipitates [28,39].

Small-Angle Neutron Scattering is a non-destructive technique for quantitative and statistically relevant precipitate characterization in steels [26,27,44-48]. By the separation of the nuclear and magnetic precipitate scattering contributions, it is possible to obtain information on the magnetic and chemical properties of the precipitates [48]. Earlier studies on the precipitation kinetics of vanadium carbides on interphase boundaries by ex-situ SANS [13,26] have been performed in low-carbon steels at room temperature. In these ex-situ SANS experiments, the microstructure is transforming from austenite to ferrite during which the vanadium carbide precipitation takes place. Subsequent quenching of the steel to room temperature results in a complex microstructure of ferrite, vanadium carbides, martensite, iron carbides and dislocations. In such ex-situ SANS measurements, it is challenging to accurately separate the precipitate signal from the interfering signal from the dislocations of the martensite.

The major advantages of performing in-situ SANS measurements which we demonstrate in this work, are: 1) the SANS signal of the precipitates is free from interference from the dislocations of the martensite and 2) an optimum background can be measured of the matrix without the presence of precipitates at temperatures where all precipitates are dissolved in the matrix. In this way, the precipitate signal can be isolated and the precipitate chemical composition can be determined. In addition, in the in-situ experiments the real-time evolution of the precipitate chemical composition can be measured. However, the SANS technique, either ex-situ or in-situ, does not provide direct information on the precipitate crystal structure, therefore, complementary techniques such as TEM or literature data are necessary to support the SANS measurements.

In this work, we study quantitatively and in real-time the chemical composition evolution of precipitates in low-carbon vanadium micro-alloyed steels using in-situ SANS. The results are supported by APT, literature data as well as ThermoCalc [49] equilibrium calculations. The effects of the processing temperature and different vanadium and carbon concentrations of each steel composition on the precipitate chemical composition evolution are investigated. The chemical composition evolution of the precipitates is determined irrespective of the precipitate shape and size distribution. The time evolution of the fraction of iron in the vanadium carbide lattice, for which limited experimental investigation has been reported so far, is derived from the in-situ SANS, together with the stoichiometry of the precipitates.

2. Experimental

The precipitate chemical composition evolution is studied in three vanadium micro-alloyed steels. The steels were provided by Tata Steel in Europe as hot-rolled plates. The chemical composition of the alloys is given in wt.% and at.% in Table 1. The steels differ in vanadium and carbon content. The first two steels have the same carbon but different vanadium contents and are referred to hereafter as LCLV (low carbon - low vanadium alloy) and LCHV (low carbon - high vanadium alloy). The third steel has a double amount of vanadium and carbon compared to the LCLV steel and is called HCHV (high carbon - high vanadium alloy). The atomic ratio of vanadium to carbon is 1 in the LCLV and HCHV steels. All steels have the same manganese concentration and the amount of the other elements is as low as possible. The LCLV and HCHV steels

Table 1
Chemical composition of the steels in weight percent (wt.%) and atomic percent (at.%) with balance Fe.

Steel		C	Mn	V	Si	P	Cr	Al
LCLV	wt.%	0.071	1.84	0.29	0.010	0.0010	0.010	0.004
	at.%	0.330	1.86	0.32	0.026	0.0018	0.011	0.008
LCHV	wt.%	0.075	1.83	0.57	0.014	0.0010	0.006	0.006
	at.%	0.350	1.85	0.62	0.028	0.0018	0.011	0.012
HCHV	wt.%	0.140	1.83	0.57	0.013	0.0010	0.007	0.008
	at.%	0.620	1.85	0.62	0.026	0.0018	0.007	0.002

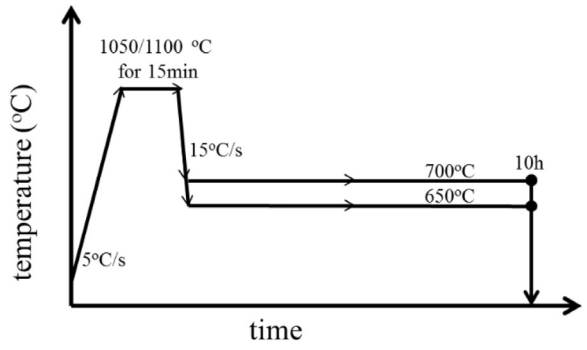

Fig. 1. Schematic illustration of the thermal cycles conducted in the furnace [50] during the in-situ SANS measurements.

will provide information on the vanadium and carbon effects when the atomic ratio of these elements is 1, whereas the LCHV steel will clarify how the excess of solute vanadium atoms influences the kinetics of the evolution of the precipitate chemical composition.

I-shaped specimens of 1 mm thickness were machined from the centre of the hot-rolled plates as in ref. [26]. The specimen shape and size was designed to fit in a furnace [50], which was used for heat-treating the specimens during in-situ SANS measurements. The furnace was custom made at Delft University of Technology, and specially designed to fit to the sample area of the Larmor Instrument at the ISIS Neutron and Muon Source (at the STFC Rutherford Appleton Laboratory), in order to perform in-situ SANS measurements. A detailed description of the instrumentation is provided in ref. [50].

The thermal cycle followed during the in-situ SANS measurements is schematically illustrated in Fig. 1. The specimens are heated up with a rate of 5 °C/s to a temperature of 1050 °C (for LCLV specimens) or 1100 °C (for LCHV and HCHV specimens) and are held there for 15 min. These temperatures are chosen to be ~50 °C higher than the respective precipitate dissolution temperatures calculated by ThermoCalc. At these soaking temperatures all elements are therefore in solid solution and the specimens are fully austenitic. Subsequently, the specimens are cooled to 650 °C or 700 °C with a rate of 15 °C/s at which temperatures austenite to ferrite phase transformation and precipitation are taking place during a 10-hour isothermal annealing treatment. Finally, the samples are cooled to room temperature.

The furnace is placed between the pole shoes of a 3473-70 GMW electromagnet, which is used to generate a vertical magnetic field of 1.5 T perpendicular to the neutron beam. This magnetic field is strong enough to saturate the magnetization of the specimens. In this way we eliminate the scattering of domains and, as explained below, we can separate the nuclear contribution to the SANS pattern from the magnetic contribution.

The size of the incident neutron beam is 8 × 8 mm^2, the wavelength range for SANS is 0.42-1.33 nm and the SANS detector is a 600 × 600 mm^2 ^{3}He tube array with an 8 × 8 mm^2 pixel size, located 4.3 m from the sample. The reduction of SANS raw data is done using the Mantid software [51].

The specimens for APT are heat-treated in a dilatometer prior to the APT investigations. The dilatometry specimens are rectangular with dimensions 14 × 10 × 1 mm^3. The equipment used is a DIL-805 A/D dilatometer with inductive heating under a low pressure of 10^{-4} mbar and cooling is achieved by helium gas. An S-type thermocouple is spot-welded in the centre of the specimen to control the temperature and monitor the thermal cycle. The same heat-treatments as the ones conducted with the use of the SANS furnace (Fig. 1) are applied, i.e., holding at 1050 °C or 1100 °C for 15 min followed by a 10 h isothermal annealing at 650 °C or 700 °C and finally quenching to room temperature.

APT measurements are performed on samples taken from the dilatometry pre-treated specimens. More than 8 tips from each condition are tested aiming for good statistics and representative results. The specimens are prepared by the lift-out method using Focussed Ion Beam milling (FIB) [52]. A LEAP 4000X-HR system from CAMECA Instruments is used for the measurements. The preparation procedure of the APT tips is described in detail in refs. [26,53]. The APT data reconstruction is performed using the IVAS 3.8.0 software from CAMECA Instruments, in which elemental ions are identified based on their isotope distribution in a time of flight mass spectrum and then the atomic arrangement of the analysed volume is reconstructed following the standard protocol [53-55].

3. Method for calculating the precipitate chemical composition evolution from the in-situ Small-Angle Neutron Scattering data

The magnetic scattering of neutrons originates only from the magnetization components that are perpendicular to the scattering vector **Q**. In our experiment we use this selection rule to separate the magnetic from the nuclear neutron scattering. For this purpose we apply in the detector plane, along the vertical direction (see Graphical Abstract and Fig. S1 in the supplementary material), a magnetic field **B** strong enough to accomplish magnetic saturation of the sample. In this case, the components of the magnetization perpendicular to **B** vanish. Thus, the magnetic scattering for **Q** // **B** is zero whereas it is maximum for **Q** ⊥ **B**. Consequently, the macroscopic differential scattering cross-section, $(d\Sigma/d\Omega)(Q)$, which is the background-corrected and calibrated SANS intensity [56], can be written as [46]:

$$\left(\frac{d\Sigma}{d\Omega}\right)(Q) = \left(\frac{d\Sigma}{d\Omega}\right)_{NUC}(Q) + \left(\frac{d\Sigma}{d\Omega}\right)_{MAG}(Q)\cdot \sin^2\alpha \quad (1)$$

where $(d\Sigma/d\Omega)_{NUC}(Q)$ and $(d\Sigma/d\Omega)_{MAG}(Q)$ stand for the nuclear and the magnetic scattering cross-sections respectively, Q is the magnitude of **Q**, and α is the angle between **Q** and **B**. $(d\Sigma/d\Omega)_{NUC}(Q)$ and $(d\Sigma/d\Omega)_{NUC}(Q)+(d\Sigma/d\Omega)_{MAG}(Q)$ are determined from the intensity integrated over sectors of 30° parallel and perpendicular to ***B***, respectively. In our case $(d\Sigma/d\Omega)_{NUC}(Q)$ is obtained from the vertical sectors and $(d\Sigma/d\Omega)_{NUC}(Q)+(d\Sigma/d\Omega)_{MAG}(Q)$ from the horizontal ones. $(d\Sigma/d\Omega)_{MAG}(Q)$ is then calculated as the difference between the above terms.

For a dilute system of precipitates within a homogeneous matrix, $(d\Sigma/d\Omega)_i(Q)$ is [56]:

$$\left(\frac{d\Sigma}{d\Omega}\right)_i(Q) = (\Delta\rho_i)^2 \int D_N(R)\cdot V^2(R)\cdot P^2(Q,R)dR, \quad (2)$$

where i can be either the nuclear or the magnetic term. R and V are the precipitate spatial coordinate in three dimensions and the precipitate volume, respectively. $D_N(R)$ is the log-normal size distribution of the precipitates and $P(Q,R)$ is the form factor reflecting the precipitate shape [56,57]. $\Delta\rho_i$ is the difference in scattering length density (scattering contrast) between the matrix and the precipitates, nuclear or magnetic. When the steel has reached magnetic saturation, the ratio of the nuclear to the magnetic SANS component is proportional to the squared ratio of the nuclear to magnetic scattering contrast:

$$\frac{\left(\frac{d\Sigma}{d\Omega}\right)_{NUC}(Q)}{\left(\frac{d\Sigma}{d\Omega}\right)_{MAG}(Q)} = \frac{(\Delta\rho_{NUC})^2}{(\Delta\rho_{MAG})^2} \quad (3)$$

This ratio is related to the composition of the microstructural features present in the sample. In the case of precipitates in a steel matrix and only if the magnetic saturation is reached, so that the

integral in Eq. (2) has the same Q-dependence for nuclear and for the magnetic scattering (same nuclear and magnetic distribution), the ratio is determined by the chemical composition of the precipitates and the presence of different types of precipitates [48]. It has been reported that the vanadium carbide precipitate composition is size dependent [21,26] and, consequently, the ratio is influenced by changes in the precipitate size distribution. APT measurements performed earlier [26-29] show the presence of iron in the precipitates, being more pronounced in the smaller precipitates. In addition, vanadium carbides with a sub-stoichiometric ratio of carbon to vanadium have been reported in the literature [5,13,21-24]. By in-situ SANS we are able to quantify the evolution of the iron content and the stoichiometry of the precipitates during annealing.

It is important to note here that since the ratio is sensitive to all microstructural features, it is critical that the experimentally determined values of both the nuclear and magnetic scattering are free from any contributions other than from the vanadium carbide precipitates (same Q-dependence of nuclear and magnetic scattering of the integral, Eq. (2)). Thus, for a quantitative analysis of the chemical composition of precipitates by SANS, it is important to fulfil the two following experimental conditions. First, measure at temperatures high enough to avoid the formation of cementite, of pearlite and in particular of martensite because in that case the SANS signal from the dislocations would interfere with the signal from the precipitates. Second, determine the SANS signal originating from the matrix without any precipitates. Both conditions have been fulfilled by our in-situ SANS measurements, as we measured at the isothermal holding temperatures of 650/700 °C and obtained the matrix background at the soaking temperatures of 1050/1100 °C, where all precipitates are dissolved in the matrix.

The scattering events at the Larmor instrument at ISIS can be recorded using event-mode data acquisition, where each neutron detection event has its own time stamp. This feature is very convenient for kinetics measurements, because it allows to re-bin the data over time slices that can be chosen after the measurement. Larger time slices provide good measuring statistics, however, shorter time slices allow the following of the kinetics with a higher temporal resolution. As the first hour of annealing is more critical for the kinetics, consecutive 5 minute time slices are chosen during the first hour at the isothermal holding temperature, while consecutive 30 minute time slices are chosen for annealing times longer than 1 h.

As a first step for determining the precipitate chemical composition evolution by in-situ SANS, the experimental $(d\Sigma/d\Omega)_{NUC}(Q)/(d\Sigma/d\Omega)_{MAG}(Q)$ ratio is calculated for all Q values in each time slice during the isothermal annealing at 650 °C and at 700 °C of the three alloy steels of interest. Due to the aforementioned advantages that the in-situ SANS measurements allow for, no considerable Q dependence of the $(d\Sigma/d\Omega)_{NUC}/(d\Sigma/d\Omega)_{MAG}$ ratio is observed in each individual time slice (see Fig. 3). A weighted average value for the $(d\Sigma/d\Omega)_{NUC}/(d\Sigma/d\Omega)_{MAG}$ is calculated for each time slice and eventually the $(d\Sigma/d\Omega)_{NUC}/(d\Sigma/d\Omega)_{MAG}$ over time is obtained.

As a second step, we assume that the SANS signal arises from precipitates with a chemical formula $(Fe_xV_{1-x-z}Mn_z)C_y$ and a NaCl type crystal structure during the entire annealing process. This hypothesis is based on literature studies of the VC_y crystal structure in low-carbon steels [5,13,21-23]. Other crystal structures for the precipitates rather than NaCl are not considered, even though they have been reported for medium carbon steels [25]. It is also possible that in the very early stage of the nucleation process, the embryos have a different crystal structure than NaCl [24], however, this is not taken into account. In the NaCl crystal structure, the Fe, V and Mn atoms can occupy the metal positions in the lattice with fractions of x, 1-x-z and z, respectively. The manganese fraction, z, is very small compared to the iron and vanadium fractions. Therefore, it is considered constant and, for each steel at a specific temperature, its value is the same as the equilibrium manganese fraction in the precipitates as derived from ThermoCalc calculations. The parameter y is the ratio of carbon, C, to metal, M, atoms, in the precipitate, i.e., C:M, and indicates deviations from the stoichiometric ratio of the carbides. For stoichiometric precipitates $y = 1$, but if vacancies are present at the carbon positions in the precipitate lattice, y is smaller than 1. In addition, if there is a single type of precipitate present in the steel with different stoichiometric ratios of carbon-to-metal, y represents the weighted average of the distribution of the carbon-to-metal ratios. The carbon-to-metal ratio is found to be related to the precipitate size distribution. For instance, in ref. [21], fine stoichiometric VC precipitates ($y = 1$) and coarse V_4C_3 ($y = 0.75$) precipitates were identified by TEM. Based on such literature findings [5,13,21-23], we consider $0.75 \leq y \leq 1$. For the ferritic matrix, z_{matrix} is the atomic fraction of manganese in the matrix which is assumed constant during annealing and equal to its nominal concentration in the alloys.

The ratio $\Delta\rho^2_{NUC}/\Delta\rho^2_{MAG}$ is theoretically calculated as a function of the precipitate chemical composition, i.e., as a function of the x and y parameters, with constant z.

The difference in the scattering length densities between the precipitates and the iron matrix is $\Delta\rho_{NUC} = \rho_{NUC\_matrix} - \rho_{NUC\_precip}$. The scattering length density of the matrix is:

$$\rho_{NUC\_matrix} = \frac{\sum_j \left(f_j^m \cdot b_j\right)}{V_{bcc}} \approx \frac{(1 - z_{matrix}) \cdot b_{Fe} + z_{matrix} \cdot b_{Mn}}{V_{bcc}} \quad (4)$$

and the precipitates' scattering length density is:

$$\rho_{NUC\_precip} = \frac{\sum_j \left(f_j^p \cdot b_j\right)}{V_{precip}} \approx \frac{x \cdot b_{Fe} + (1 - x - z) \cdot b_V + z \cdot b_{Mn} + y \cdot b_C}{V_{precip}} \quad (5)$$

where j stands for each individual element in the phase: j = Fe, Mn, V or C, and f_j^m and f_j^p are the atomic fractions of each element in the matrix and the precipitate unit cell, respectively. The V_{bcc} is the atomic volume of the matrix and the V_{precip} the atomic volume of the substitutional elements in the precipitates. They are calculated as: $V_{bcc} = a^3_{bcc}/2$ and as $V_{precip} = a^3_{precip}/4$. The a_{bcc} and the a_{precip} are the lattice parameters of the ferrite unit cell and of the precipitate unit cell. The lattice parameter dependence on temperature is considered for both precipitates [58] and matrix [59]. For the precipitates, the additional dependence of the lattice parameter on the precipitate stoichiometry, i.e. on the carbon vacancies fraction, is also taken into account in the calculations [60]. The numbers 2 and 4 used for the atomic volume of the matrix and the precipitates calculation, respectively, are the total number of metal atoms in the BCC ferrite matrix unit cell and in the precipitate unit cell. The b_j is the coherent scattering length of each element j [61]. The coherent scattering lengths are $b_{Fe} = 9.45 \times 10^{-15}$ m for iron, $b_C = 6.646 \times 10^{-15}$ m for carbon, $b_V = -0.3824 \times 10^{-15}$ m for vanadium and $b_{Mn} = -3.73 \times 10^{-15}$ m for manganese. The vanadium and carbon fractions in solid solution in the matrix are excluded from the matrix contrast calculation because of their insignificant numerical contribution.

Similar to the nuclear contrast between the matrix and the precipitates, the magnetic contrast is $\Delta\rho_{MAG} = \rho_{MAG\_matrix} - \rho_{MAG\_precip}$. The matrix magnetic scattering length is:

$$\rho_{MAG\_matrix} = \frac{p}{V_{bcc}} \quad (6)$$

In the ferritic matrix only the Fe is magnetic and the p parameter in Eq. (6) is its magnetic scattering length given by $p = 2.699 \times 10^{-15}\text{m} * \mu$, where μ is the saturation per iron atom in μ_B units. The magnetization saturation temperature dependence

Table 2
Equilibrium precipitate chemical composition predicted by ThermoCalc.

Steel	annealing temperature (°C)	at.% of atoms in the precipitates				precipitates' chemical formula
		at.%V	at.%C	at.%Fe	at.%Mn	$(Fe_xV_{1-x-z}Mn_z)C_y$
LCLV	650	44.75	46.58	8.35	0.31	$(Fe_{0.156}V_{0.84}Mn_{0.006})C_{0.872}$
	700	46.18	46.49	7.10	0.23	$(Fe_{0.133}V_{0.86}Mn_{0.004})C_{0.869}$
LCHV	650	51.65	45.62	2.66	0.06	$(Fe_{0.049}V_{0.95}Mn_{0.001})C_{0.839}$
	700	51.39	45.74	2.80	0.07	$(Fe_{0.050}V_{0.95}Mn_{0.001})C_{0.843}$
HCHV	650	45.72	46.54	7.48	0.25	$(Fe_{0.140}V_{0.86}Mn_{0.005})C_{0.871}$
	700	46.29	46.49	6.99	0.23	$(Fe_{0.130}V_{0.87}Mn_{0.004})C_{0.869}$

is taken into consideration as in ref. [62] and is equal to 1.47 μ_B at 650 °C (corresponding to $\mu_0{}^*M$ ~ 1.45 T, where μ_0 is the magnetic permeability of the vacuum and M the magnetization) and to 1.26 μ_B at 700 °C (corresponding to $\mu_0{}^*M$ ~ 1.24 T) resulting to a magnetic scattering length of 3.97 × 10^{-15} m at 650 °C and 3.39 × 10^{-15} m at 700 °C.

The magnetic scattering from the precipitates depends on the fraction of Fe in the precipitates and the corresponding magnetic scattering length is:

$$\rho_{MAG\_precip} = x \cdot \frac{p}{V_{precip}} \tag{7}$$

By combining Eq. (4)-(7), for each steel composition and for a specific temperature, 650 °C or 700 °C, the $\Delta\rho^2_{NUC}/\Delta\rho^2_{MAG}$ is obtained as a function of the x and y, i.e., as a function of the precipitate chemical composition. Following Eq. (3), the experimental intensity ratio evolution for each time slice is thus obtained as a function of x and y:

$$\frac{\left(\frac{d\Sigma}{d\Omega}\right)_{NUC}}{\left(\frac{d\Sigma}{d\Omega}\right)_{MAG}} = \frac{\left(\frac{(1-z_{matrix})\cdot b_{Fe}+z_{matrix}\cdot b_{Mn}}{V_{bcc}} - \frac{x\cdot b_{Fe}+(1-x-z)\cdot b_V+z\cdot b_{Mn}+y\cdot b_C}{V_{precip}}\right)^2}{\left(\frac{p}{V_{bcc}} - x\cdot\frac{p}{V_{precip}}\right)^2} = f(x,y) \tag{8}$$

The presence of iron in the precipitates reduces both $\Delta\rho^2_{NUC}$ and $\Delta\rho^2_{MAG}$. However, the decrease in $\Delta\rho^2_{NUC}$ is much larger, causing an overall reduction of $\Delta\rho^2_{NUC}/\Delta\rho^2_{MAG}$. On the other hand, the presence of carbon vacancies leads to an increase of $\Delta\rho^2_{NUC}/\Delta\rho^2_{MAG}$. Consequently, different combinations of x and y can result in the same ratio of the nuclear-to-magnetic macroscopic differential scattering cross-sections as given by Eq. (8). In order to overcome this complication and due to the fact that the precipitate composition can be assumed to reach a plateau after 10 h of annealing according to the experimental SANS intensity ratios (as will be shown in the Figs. 4-6 of the present study), the ThermoCalc software is used to determine the equilibrium precipitate stoichiometry.

ThermoCalc equilibrium calculations of the precipitates chemical composition are performed for the three alloys at 650 °C and at 700 °C. The results are listed in Table 2. In equilibrium, in all alloys and at both temperatures, the precipitates are mainly vanadium carbides with less than 8.5% of iron and an even smaller fraction of manganese (less than 0.5%) present. According to ThermoCalc, the equilibrium precipitate chemical composition in LCLV and HCHV steels is very similar. In the LCHV steel at both temperatures the concentration of iron and manganese in the precipitates is less than the corresponding concentrations in the precipitates in the LCLV and HCHV steels.

In the last column of Table 2, the precipitate stoichiometry is presented based on the carbon-to-metal fraction as derived from ThermoCalc. For solving Eq. (8), the y value for each steel at a specific temperature is assumed to be constant during annealing, and equal to the equilibrium value given by ThermoCalc. Then the fraction of iron in the precipitates during annealing is obtained from Eq. (8) and the fraction of vanadium is the remaining metallic fraction after the subtraction of iron and manganese fractions.

However, the validity of the assumption that y remains overall constant during annealing, is questionable because it basically implies that the precipitate (sub-)stoichiometry distribution is time-independent. Moreover, y may also change with time because it may be dependent on the size of the precipitates and the size distribution changes with time. The time evolution of the precipitate sub-stoichiometry distribution is included in the final chemical composition calculations by calculating boundaries for the iron and vanadium fractions. Since a decrease of y and a decrease in the amount of iron in the precipitates both result in an increase in the $\Delta\rho^2_{NUC}/\Delta\rho^2_{MAG}$ ratio, by solving Eq. (8) for a given experimental ratio, y_{min} = 0.75 will determine the upper boundary for the Fe fraction. Accordingly, y_{max} = 1 will yield the lower boundary for the Fe fraction. The boundaries in the fraction of vanadium are calculated as the boundaries of iron subtracted from 1 for each moment of annealing.

Summarizing, following this method, the precipitate chemical composition evolution can be calculated for any steel composition and for all possible precipitate sizes and shapes without fitting of any parameters other than the composition parameters (e.g. parameters related to the precipitates size distribution). The complexity, however, of the analysis increases when more alloying elements that can partially substitute vanadium in the vanadium carbide precipitate are included, or when different types of precipitates with different size distribution evolution are present. Moreover, a limitation of the SANS technique is that it cannot directly provide information on the precipitate crystal structure and on the spatial distribution of the metal atoms within the precipitate. For these reasons, complementary techniques like TEM and APT should accompany and complement the SANS measurements.

4. Results and Discussion

4.1. Small-Angle Neutron Scattering

All nuclear and magnetic differential scattering cross-sections of the LCLV, LCHV and HCHV steels obtained by in-situ SANS during annealing at 650°C and at 700 °C are presented in the supplementary material of this paper (Fig. S2). Because of space limitations, only an example, the differential scattering cross-section evolution in the LCLV during annealing at 650 °C is shown in Figs. 2a and 2b for the nuclear and the magnetic components, respectively. These curves are obtained after background subtraction, and therefore consist only of the precipitation scattering contribution. The subtracted background signal consists of the furnace scattering contribution and the scattering from a steel without precipitates (obtained from the scattering of the samples at the soaking temperature, 1050 °C or 1100 °C). The SANS intensity during cooling (obtained by using 1 minute time slices) is compared to the SANS signal at high temperatures and the curves are identical, indicating

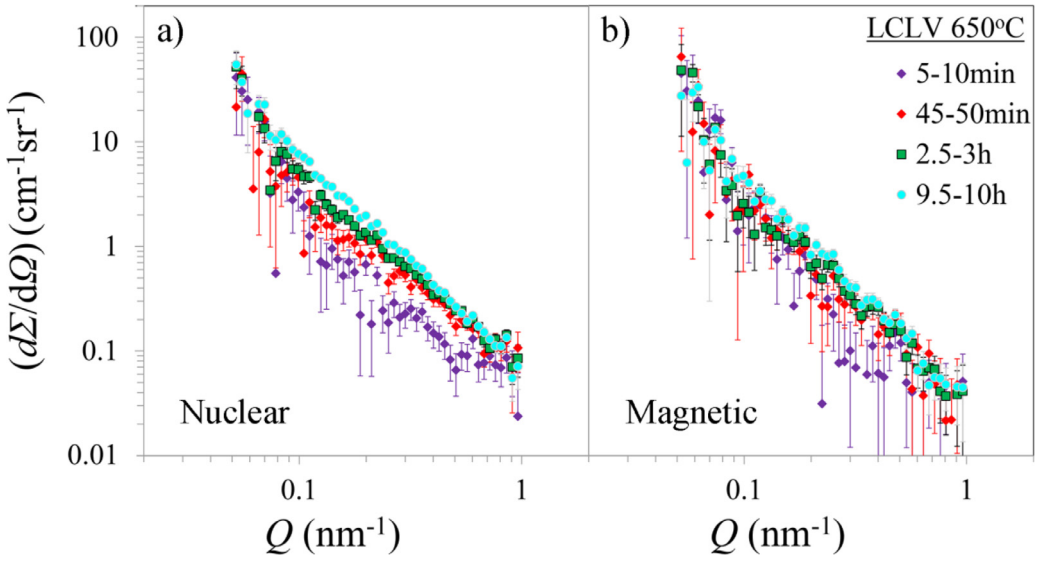

Fig. 2. a) Nuclear and b) magnetic differential scattering cross sections obtained during annealing of LCLV steel at 650 °C as a function of *Q*. The scattering curves of some selected annealing times are shown.

that no precipitation takes place before the isothermal annealing temperature is reached.

Four representative time slices are chosen and the SANS intensity time evolution during isothermal holding is shown in Fig. 2. Both nuclear and magnetic intensities are increasing with time due to precipitation, and the magnitude of intensity increase depends on the volume fraction of the precipitates formed. The intensity increases more rapidly during the first hour of annealing, indicating faster precipitation kinetics at the beginning of annealing than at later stages. The intensity curves corresponding to shorter annealing times have larger error bars due to the re-binning of data over shorter time slices than for the long annealing times.

Note that for short annealing times the precipitate size and volume fraction are small, therefore the measured scattering intensity is low. In addition, the *Q*-range of the Larmor instrument is limited, affecting the accuracy in resolving the smallest precipitates. However precipitates of size of ~1 nm can be detected as stated in ref. [26].

Fig. 3 provides the $(d\Sigma/d\Omega)_{NUC}/(d\Sigma/d\Omega)_{MAG}$ ratios obtained by in-situ SANS measurements on the LCLV steel annealed at 650 °C. The ratio is calculated from the scattering curves of Figs. 2a and 2b. Note that the errors for short annealing times are relatively large due to the limited counting statistics. Since we observe no significant *Q*-dependence we calculate the weighted average for the $(d\Sigma/d\Omega)_{NUC}/(d\Sigma/d\Omega)_{MAG}$ ratio over *Q* for each time slice. The weighted average is calculated as the $\sum_{n=1}^{npts}((1/r^2_{error,n})\cdot r_n)/\sum_{n=1}^{npts}(1/r^2_{error,n})$, where n stands for each individual data point in Fig. 3, r_n and $r_{error,n}$ are the experimental $((d\Sigma/d\Omega)_{NUC}/(d\Sigma/d\Omega)_{MAG})(Q)$ ratio and its error for each *Q*, respectively, and npts is the number of the experimental data points. The dotted lines in Fig. 3 represent the calculated weighted average of the nuclear to magnetic intensity ratio for each time slice. The ratio is increasing during annealing of all the steels at both 650 °C and 700 °C and it is presented later in Figs. 4a-b, 5a-b and 6a-b.

Examples of nuclear and magnetic differential scattering cross sections vs *Q* of all steels annealed at 650 °C and 700 °C are provided in the supplementary material (Fig. S3), showing the *Q* independence of the $(d\Sigma/d\Omega)_{NUC}/(d\Sigma/d\Omega)_{MAG}$ ratio.

The experimental, weighted averaged, $(d\Sigma/d\Omega)_{NUC}/(d\Sigma/d\Omega)_{MAG}$ ratio evolution during annealing at 650 °C and at 700 °C is presented for the LCLV, LCHV and HCHV steels in the graphs of Figs. 4a-b, 5a-b and 6a-b, respectively. The missing points in the graphs are due to an interruption of the neutron beam. The errors in the experimental $(d\Sigma/d\Omega)_{NUC}/(d\Sigma/d\Omega)_{MAG}$ ratio are statistical errors originating from the neutron measurements.

For all steels and at both temperatures, the $(d\Sigma/d\Omega)_{NUC}/(d\mathbf{\Sigma}/d\Omega)_{MAG}$ ratio increases during annealing, indicating changes in the precipitate chemical composition with time. As shown in Figs. 4-6, the first 4 hours are the most critical for the precipitate chemical composition evolution while at the later stages of annealing, the $(d\Sigma/d\Omega)_{NUC}/(d\Sigma/d\Omega)_{MAG}$ ratio reaches a plateau value suggesting that the (metastable) equilibrium precipitate composition is reached. The smaller experimental $(d\Sigma/d\Omega)_{NUC}/(d\Sigma/d\Omega)_{MAG}$ ratio in the first hours of annealing is mainly attributed to the presence of iron in the precipitates which, as explained in the previous section, leads to a lower $\Delta\rho^2{}_{NUC}/\Delta\rho^2{}_{MAG}$.

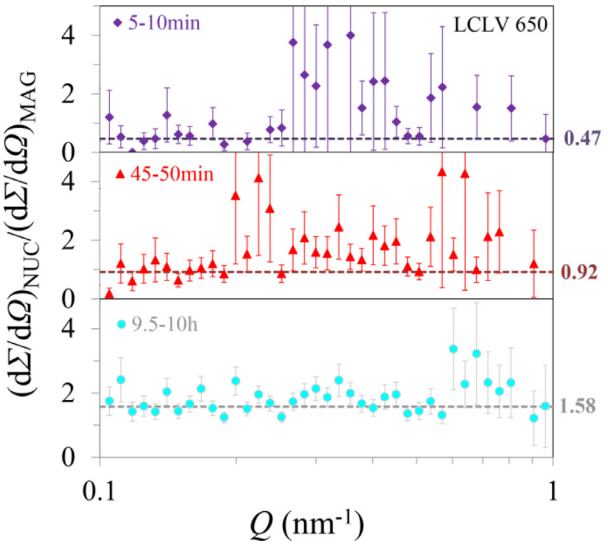

Fig. 3. Ratios of the nuclear to magnetic scattering cross sections plotted versus the scattering vector, *Q*, on a logarithmic scale, for LCLV alloy samples annealed at 650 °C for different annealing times from the in-situ scattering curves of Figs. 2a and b.

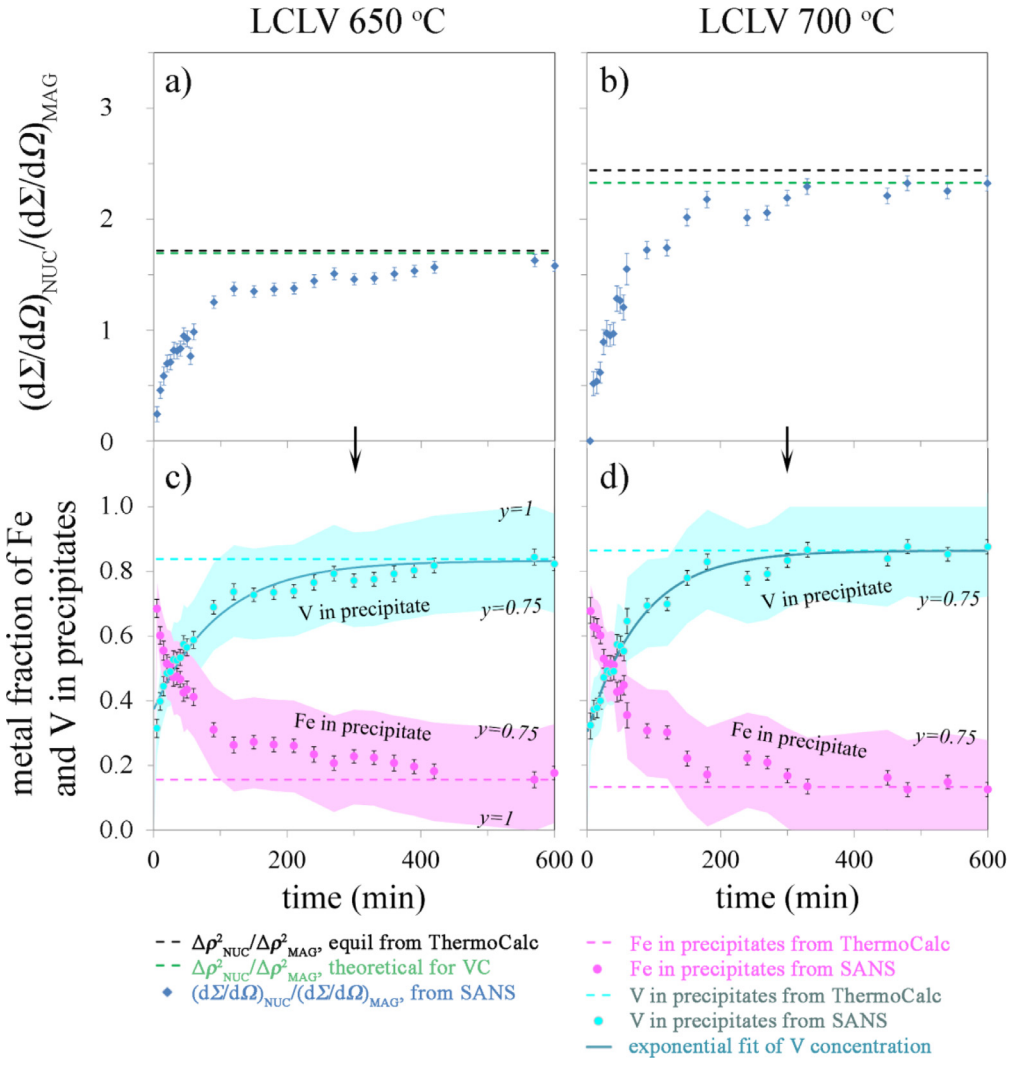

Fig. 4. Experimentally observed evolution of the ratio of the nuclear to magnetic scattering cross section of the LCLV steel during annealing a) at 650 °C and at b) 700 °C. The derived precipitate composition evolution is shown in c) and d), respectively. The solid lines in the figure c and d are fits with Eq. (9).

The black dashed horizontal line plotted in Figs. 4a-b, 5a-b and 6a-b is the $\Delta\rho^2_{NUC}/\Delta\rho^2_{MAG}$ ratio that corresponds to the equilibrium precipitate chemical composition according to ThermoCalc (presented in Table 2). The green dashed horizontal line is the theoretically calculated $\Delta\rho^2_{NUC}/\Delta\rho^2_{MAG}$ ratio for stoichiometric vanadium carbides that do not contain any iron but only a small fraction of manganese given by ThermoCalc. This ratio (for stoichiometric vanadium carbides) is temperature dependent and is equal to 1.69 at 650 °C and 2.33 at 700 °C. Both $\Delta\rho^2_{NUC}$ and $\Delta\rho^2_{MAG}$ are lower at 700 °C than at 650 °C, but the $\Delta\rho^2_{MAG}$ reduction is stronger due to the reduction in the magnetization of the iron matrix at 700 °C compared to that at 650 °C. ThermoCalc indicates a sub-stoichiometric equilibrium precipitate composition for all steels ($y < 1$) and this is graphically shown by the black line having a higher value than the green stoichiometric line for which $y = 1$. The fact that we measure ratios above the corresponding ratio for pure vanadium carbide (green lines), especially in the cases of LCHV and HCHV at both temperatures, is a strong indication for the presence of sub-stoichiometric carbides.

For the HCHV steel at both annealing temperatures, the experimental $(d\Sigma/d\Omega)_{NUC}/(d\Sigma/d\Omega)_{MAG}$ ratio is larger than the equilibrium and the stoichiometric ratios (Figs. 6a and 6b), implying that the carbon-to-metal ratio in the precipitates of this steel is smaller than the ThermoCalc results. For this steel, a red dashed horizontal line is plotted corresponding to $(V,Fe,Mn)_4C_3$ for comparison.

In order to quantify the evolution of iron and vanadium fractions in the precipitates, we follow the method described in Section 3. The results are presented in Figs. 4c-d, 5c-d and 6c-d for the three steels. The marker dots for the iron and vanadium fractions result from the solution of Eq. (8) using y from ThermoCalc for each steel at each temperature. The error bars reflect the statistical error from the SANS measurements. They are calculated from the experimental $(d\Sigma/d\Omega)_{NUC}/(d\Sigma/d\Omega)_{MAG}$ ratio errors, after solving Eq. (8). The shaded areas in the iron and vanadium fractions reflect the spread in the iron and vanadium fractions in the precipitates during annealing when the upper ($y_{max} = 1$) and lower ($y_{min} = 0.75$) values for y are applied to Eq. (8). The iron and vanadium fractions can vary between 0 and 1, setting the upper boundary for y during annealing (boundaries in the shaded areas in Figs. 4-6). According to Figs. 4-6, the precipitates in the LCLV steel at both temperatures tend to a more stoichiometric distribution than the LCHV and HCHV steels, indicated by the larger y values.

For the HCHV steel annealed at 700 °C, $y = 0.869$ is given by ThermoCalc. However, by applying our method, the calculated iron and vanadium fractions in the precipitates are physically possible only for the first hours of annealing. $y = 0.869$ yields a negative iron fraction and a vanadium fraction larger than 1 after 300 min

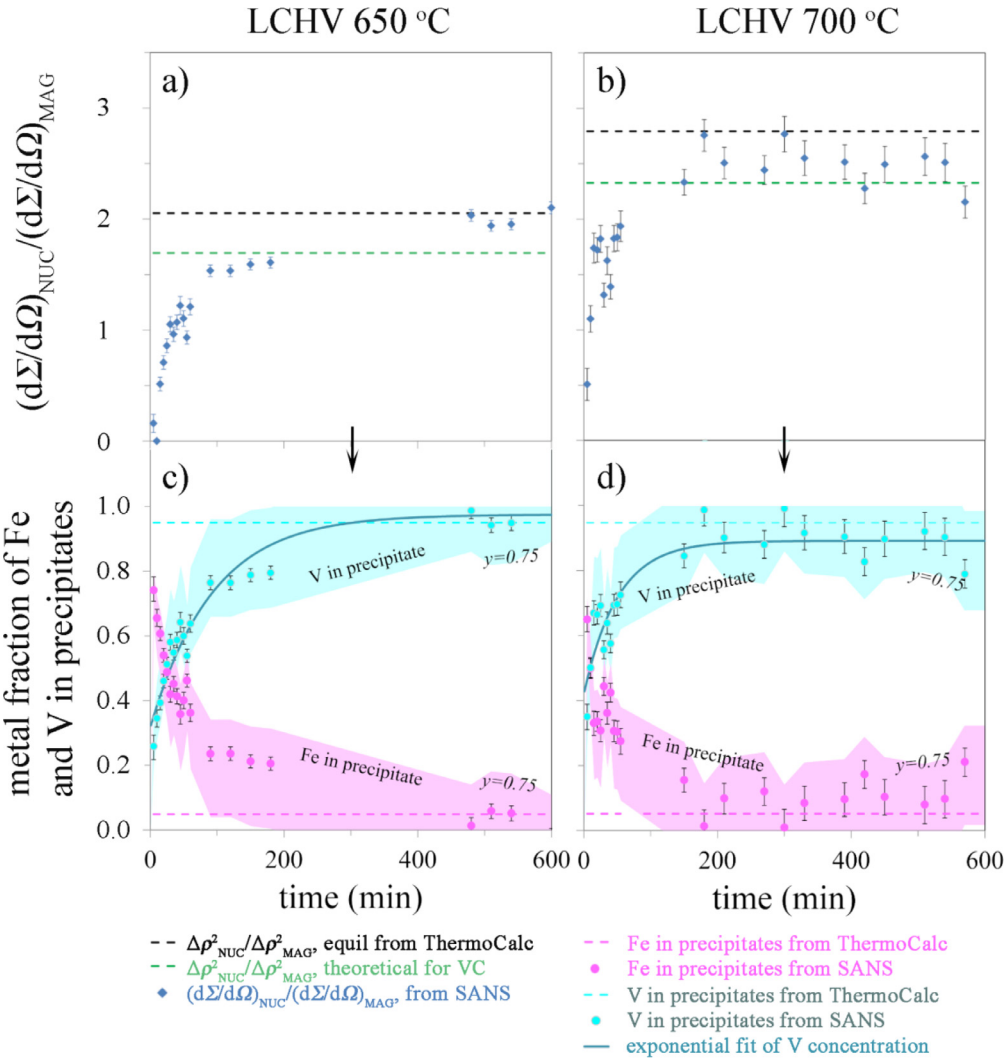

Fig. 5. Experimentally observed evolution of the ratio of the nuclear to magnetic scattering cross section of the LCHV steel during annealing a) at 650 °C and at b) 700 °C. The derived precipitate composition evolution is shown in c) and d), respectively. The solid lines in the figure c and d are fits with Eq. (9).

of annealing (Fig. 6d). This means that, either ThermoCalc gives a larger value for y than the experimental one from SANS (the final experimental $(d\Sigma/d\Omega)_{NUC}/(d\Sigma/d\Omega)_{MAG}$ ratio can be reached if the carbon-to-metal ratio is set to $y = 0.75$ in the model – Fig. 6d), or that in the HCHV steel the precipitates possibly have a different crystal structure than that of the precipitates in the steels with the lower carbon concentration (LCLV and LCHV steels). However, evidence of a different precipitate crystal structure in the precipitates of the HCHV steel is not pronounced at 650 °C. The evolution of the iron and vanadium content in the precipitates in the HCHV steel at 700 °C is calculated only for the first 300 min of annealing. The presence of metastable precipitates that have not yet reached the equilibrium precipitate composition is a possible reason for the difference between the precipitate chemical composition measured experimentally and the one given by ThermoCalc according to ref. [14].

The iron fraction in the precipitates decreases with time, with the iron being substituted by vanadium in the precipitate lattice, so that the fraction of vanadium in the precipitates is increasing with time. Since the precipitate size is becoming larger during isothermal holding (precipitate growth and coarsening), our analysis confirms the presence of iron in small vanadium carbides, in agreement with ref. [26]. Comparing the precipitate chemical composition evolution plots for the precipitates in the LCLV and LCHV steels (Figs. 4 and 5), we conclude that the addition of vanadium to the steel nominal composition leads to the formation of precipitates with a higher vanadium concentration. At both temperatures, more vanadium is included in the precipitates of LCHV and HCHV steels than in the LCLV steel as there is twice the amount of vanadium in the steels' nominal composition. Consequently, the addition of vanadium to the steel nominal composition enhances the presence of vanadium rich precipitates, with less iron and a smaller carbon to metal ratio.

These precipitates are initially metastable with a high iron concentration and their composition gradually evolves towards equilibrium during annealing. Similar conclusions are reported in [15,16] regarding the presence of iron in niobium carbides. A possible reason for the presence of iron is that it lowers the precipitate strain energy through the precipitate-matrix lattice misfit reduction, resulting in a higher net driving force (the sum of the chemical free energy difference and the strain energy) and therefore reduced activation energy for precipitate nucleation as explained in [29] for (Ni,Al,Mo) precipitates and in [15,16] for niobium carbides. Quantitatively, the average metal fraction of iron in the precipitates in all steels reduces from a value larger than 0.65 in the initial stage of precipitation to a value smaller than 0.15 in the later stages. In the LCHV steel, both at 650 and at 700 °C, the final fraction of iron in the precipitates is much less (and the amount of

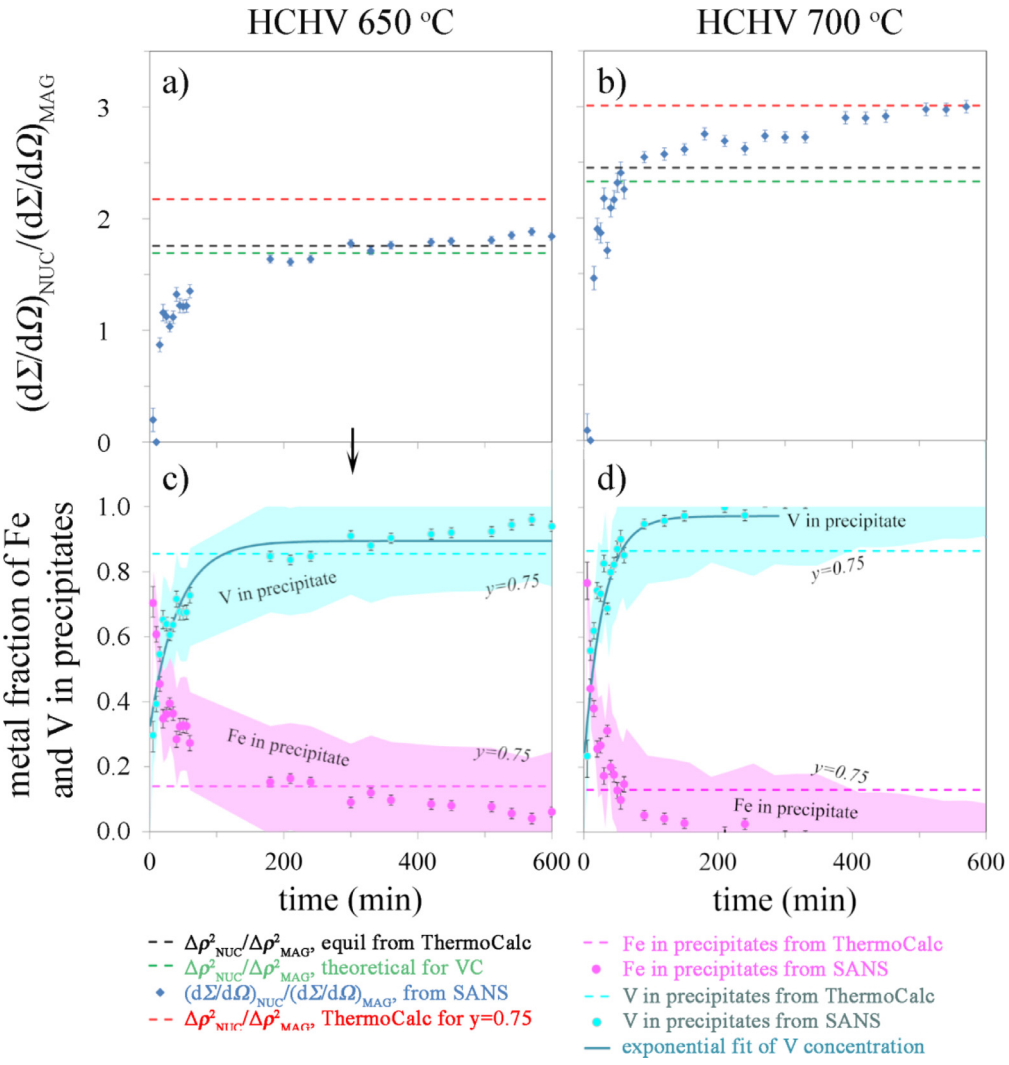

Fig. 6. Experimentally observed evolution of the ratio of the nuclear to magnetic scattering cross section of the HCHV steel during annealing a) at 650 °C and at b) 700 °C. The derived precipitate composition evolution is shown in c) and d), respectively. The solid lines in the figure c and d are fits with Eq. (9).

vanadium is much higher) than the corresponding fraction in the LCLV steel. This composition effect is a purely thermodynamic effect, as it is also shown in the equilibrium precipitate composition provided by ThermoCalc (Table 2).

It is important to note that, despite the fact that in the LCLV and HCHV steel the vanadium and carbon have the same atomic ratio (equal to 1) in the nominal composition and that ThermoCalc predicts the same precipitate composition in these two steels, the experimentally measured precipitate composition differs between the LCLV and HCHV alloys. This, in turn, could affect the resulted precipitation and modulus strengthening of the steel.

4.2. Rate of change in the precipitate chemical composition evolution by SANS

In order to calculate the rate of change in the precipitate chemical composition in the three steels, the calculated fraction of vanadium in the precipitates is fitted to the following equation:

$$V_{metal\_fraction}(t) = A - B \cdot \exp(-k \cdot t), \quad (9)$$

where A and B are fitting parameters dependent on the matrix and precipitate composition and on the annealing temperature. The k factor describes the rate of change in the precipitate chemical composition and t is the time. The fitting curves are shown in Fig. 4c-d, 5c-d, 6c-d and in Fig. 7a-b and the k factor is graphically presented for the three steels annealed at 650 °C and at 700 °C in Fig. 8.

Figs. 7a and 7b show the evolution of the metal fraction of vanadium in the precipitates during annealing at 650 °C and at 700 °C, respectively. The individual points are obtained from the experimental data after solving Eq. (8) using the y-value from ThermoCalc as explained above. These points are also presented in Figs. 4c-d, 5c-d and 6c-d. The dashed lines result from the fitting of these data points, i.e., from the fitting of the fraction of vanadium in the precipitates (Eq. (9)).

At a fixed temperature, 650 °C or 700 °C (Fig. 7a and 7b, respectively), changes in the precipitate chemical composition are faster in the LCHV and HCHV steels due to their excess of vanadium with respect to LCLV steel. This is reflected also in the larger k factor for LCHV and HCHV compared to the LCLV steel at a specific temperature (Fig. 8). The carbon has also an accelerating effect on the kinetics of evolution of the precipitate chemical composition at both temperatures (Figs. 7a and 7b). This is visible also by the larger k factor in the HCHV than in the LCLV and LCHV steels (Fig. 8).

As shown in Fig. 8, the k factor is larger at 700 °C than at 650 °C for all steels corresponding to faster changes in the precipitate chemical composition at 700 °C, which can be attributed to a faster –thermally activated– vanadium diffusion. According to Fig. 8, the influence of temperature in the rate of change in the precipitate

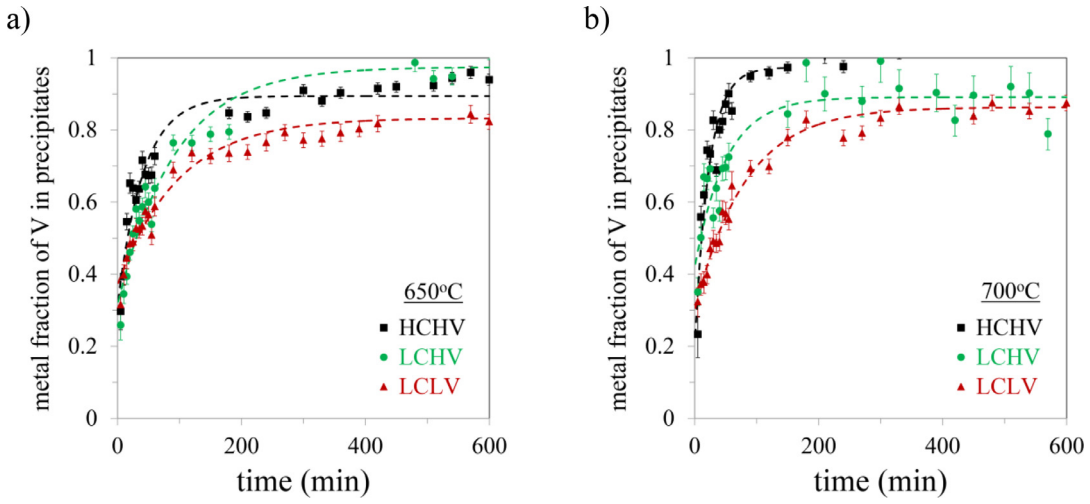

Fig. 7. Evolution of the metal fraction of vanadium in the precipitates in the LCLV(▲), LCHV(●) and HCHV(■) steels during annealing at a) 650 °C and b) 700 °C. The marker dots are obtained from the experimental data after solving Eq. (8) using the y from ThermoCalc (they are also presented in Figs. 4c-d, 5c-d and 6c-d), and the dashed lines result from the fitting of these data points, i.e., from the fitting of the amount of vanadium in the precipitates.

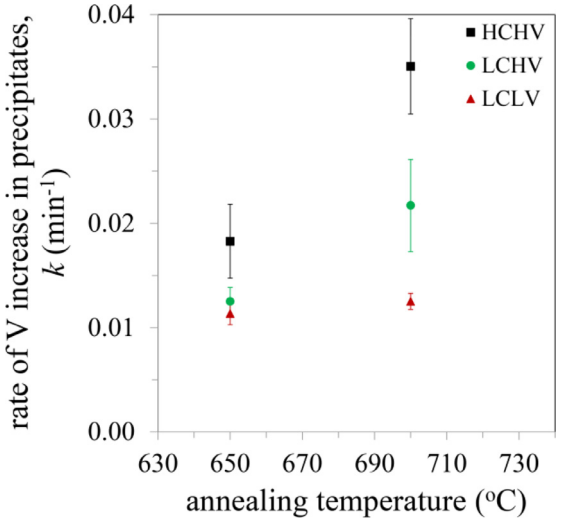

Fig. 8. Precipitate chemical composition evolution rate at 650 °C and at 700 °C for the precipitates in the LCLV, LCHV and HCHV.

chemical composition in the LCHV and HCHV steels clearly increases with increasing temperature. In the LCLV steel, the rate of change in the precipitate chemical composition increases with increasing temperature as well, however, the influence of temperature is smaller in this steel, suggesting that the impact of the increased vanadium diffusion is more evident in steels with a higher vanadium fraction.

The driving force for the precipitation of vanadium carbides in ferrite at 650 °C and at 700 °C is calculated using ThermoCalc ortho-equilibrium calculations. The results are listed in Table 3. For each steel, the driving force for precipitation is smaller at 700 °C than at 650 °C as expected due to the increase in the solubility of the precipitates when the temperature increases [9,63], and comparable to the values reported in [63].

The nucleation rate of the precipitates depends on the driving force for precipitation as described by [64]:

$$\dot{N} \propto \exp\left(-\frac{\Delta G^* + Q_D}{k_B T}\right) \tag{10}$$

In Eq. (10), Q_D is the activation energy for vanadium diffusion, T is the temperature, k_B is the Boltzmann constant and ΔG^* is the activation energy for the nucleation of the precipitates given by:

$$\Delta G^* = \frac{\Psi}{(\Delta G_V - g_s)^2} \tag{11}$$

where ΔG_V is the chemical driving force for the nucleation of the precipitates and g_s is the misfit strain energy between the precipitates and the matrix. The Ψ parameter is equal to [65]:

$$\Psi = \frac{4}{27 z_V^2}\left(\sum_l z_A^l \sigma_l\right)^3 \tag{12}$$

and it contains information about the energies, σ, between the interfaces l that are involved in the nucleation process and the shape of the critical nucleus (reflected by the coefficients $z_A{}^l$ and $z_V{}^l$) [65]. The Ψ parameter is dependent on the coherency of the precipitate/matrix interface, therefore, dependent on the iron content

Table 3
Driving force for precipitation in ferrite and precipitate dissolution temperature in the three steels of interest according to ThermoCalc.

Steel	driving force for precipitation in ferrite, ΔG_V		precipitate dissolution temperature in ºC
	annealing at 650 ºC	annealing at 700 ºC	
LCLV	24.3 kJ/mol (=2229 MJ/m^3)	21.0 kJ/mol (=1925 MJ/m^3)	990
LCHV	26.9 kJ/mol (=2462 MJ/m^3)	23.7 kJ/mol (=2173 MJ/m^3)	1060
HCHV	28.8 kJ/mol (=2642 MJ/m^3)	25.8 kJ/mol (=2361 MJ/m^3)	1069

in the precipitates due to the fact that the presence of iron in the precipitates can reduce the precipitate/matrix lattice misfit [15,16]. Consequently, because a higher fraction of iron in the precipitates increases the coherency of the precipitates and thus reduces the interfacial energy between the precipitates and the matrix, it eventually reduces Ψ. This leads to a decrease in the activation energy for the precipitate nucleation, ΔG^*, and consequently to an increase in the nucleation rate, $\dot{N}$ Eq. (10)-((12)). In addition, the presence of iron in the precipitates reduces the strain energy between the precipitate and the matrix, g_s, which, based on Eq. (11), also reduces the activation energy for the precipitate nucleation, ΔG^*, and, increases $\dot{N}$, explaining that the presence of iron in the precipitates in the first stages of annealing is critical for the entire nucleation process. The presence of iron in the precipitates affects also the chemical driving force for the nucleation, ΔG_V. Iron in the precipitates reduces ΔG_V and consequently the nucleation rate, $\dot{N}$ Eqs. (10) and ((11)). Our observations seem to favour iron-rich precipitates in the beginning of annealing, indicating that the latter effect of iron on reducing the chemical driving force and consequently reducing the $\dot{N}$ is minor compared to its effect on reducing the lattice misfit and the strain energy and consequently increasing the $\dot{N}$. The presence of carbon vacancies in the precipitates has also an influence on the driving force for precipitation and the nucleation rate through the parameters of Eq. (10), (11) and (12), however, these effects are not quantified here because of the lack of sufficient data.

Based on Eqs. (10) and (11), the smaller driving force for precipitation, ΔG_V, at 700 °C in all steels (Table 3) results in a higher activation energy for the precipitate nucleation, ΔG^*, and therefore to a reduced nucleation rate, $\dot{N}$.

Precipitates nucleate at a lower rate at 700 °C than at 650 °C [63] (see also the APT results below) but due to the larger mobility of the precipitating elements at 700 °C, the precipitate growth rate is larger at 700 °C and therefore faster changes in the precipitate chemical composition are observed at this temperature (the k factor is larger Fig. 8).

By increasing the vanadium content in the steel at a certain temperature (see the comparison between LCLV and LCHV steels in Table 3), the driving force for vanadium carbide precipitation becomes larger (in agreement with [22] and [63]) at both temperatures. This is attributed to the fact that the addition of vanadium to the steel results in an increased concentration of vanadium at the α/γ interface due to the solute drag effect.

We observe that an increase in the overall carbon concentration leads to an increase in the rate of change in the precipitate chemical composition. A possible explanation for this observation is as follows. The bulk carbon content also affects the precipitation driving force. The carbon addition also increases the precipitate dissolution temperature (Table 3 – comparison between LCHV and HCHV, consistent with [63]). However, a larger carbon content in the steel composition may retard the austenite-to-ferrite phase transformation due to the carbon enrichment in austenite [26] and consequently it might be possible that the vanadium segregation and supersaturation at the α/γ interface is enhanced, causing an increase in the driving force for precipitation (Table 3 – comparison between LCHV and HCHV) and consequently an increase in the rate of change in the precipitate chemical composition. However, the latter needs to be verified experimentally.

The values for the driving force for precipitation presented in Table 3 are based on the assumption that the vanadium carbide precipitation takes place in the bulk ferrite. In reality, these values can be different when the precipitates nucleate during the austenite-to-ferrite phase transformation in the moving α/γ boundary, in which the local concentration of the elements is somewhat different.

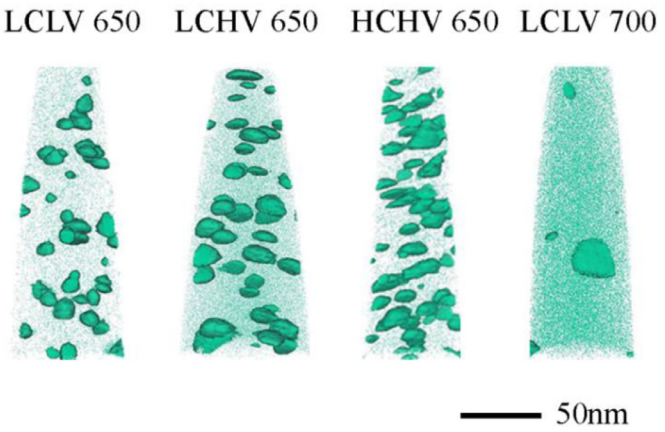

Fig. 9. From left to right: 3D APT maps of V atoms in LCLV, LCHV and HCHV after annealing at 650 °C for 10 h, and of LCLV after annealing at 700 °C for 10 h. The maps are superimposed with 2at.%V iso-concentration surfaces.

Summarizing, the alloying additions of vanadium or carbon to the steel nominal composition can increase the driving force for precipitation at a specific temperature. The rate of change in the precipitate chemical composition depends on the driving force for precipitation (which is influenced by the alloy composition, the concentration of elements at the α/γ interface, the solute drag effect and the precipitate chemical composition) as well as on the diffusivity of the precipitating elements as vanadium through their effect on the precipitate/matrix interface velocity. For each steel annealed at a specific temperature, the parameter that has the dominant effect over the others is the one that eventually controls the rate of change in the precipitate chemical composition.

4.3. Precipitate chemical composition determined by Atom Probe Tomography

Fig. 9 shows representative 3D vanadium atom maps for LCLV, LCHV and HCHV steel tips measured by APT. All maps are superimposed with 2 at.%V iso-concentration surfaces. Vanadium rich regions are clearly distinguished in all tips and correspond to vanadium carbides since carbon enrichment is also measured in these regions (an example is provided in Fig. S4 in the supplementary material of this paper). The first three maps belong to LCLV, LCHV and HCHV specimens isothermally annealed in the dilatometer at 650 °C for 10 h. Spherical/slightly ellipsoidal precipitates larger than 2 nm have been formed after 10 h at 650 °C in all steels. Much larger precipitates are seen after 10 h at 700 °C in all steels. A representative example of a tip of a LCLV specimen annealed at 700 °C for 10 h is shown in the fourth tip of Fig. 9.

Proximity Diagrams (proxigrams) [66] calculated using iso-concentration surfaces (iso-surfaces) of 2 at.%V are used to provide the precipitates' chemical composition profile. After 10 h of isothermal holding at 650 °C or at 700 °C, the precipitates have reached a stable composition according to SANS (Figs. 4-6). The precipitate chemical composition analysis is performed by the use of proxigrams in all steels after 10 h of annealing.

As a representative example, the radially averaged 1D composition profiles of two precipitates in the LCHV steel annealed at 700 °C for 10 h are shown in Figs. 10a and 10b. More composition profiles of precipitates in LCLV, LCHV and HCHV steels can be found in the supplementary material (Figs. S5-S7). No manganese enrichment is measured by APT in the precipitates in any of the three alloy steels in agreement with ThermoCalc calculations, therefore the amount of manganese is not plotted in the proxigrams for the

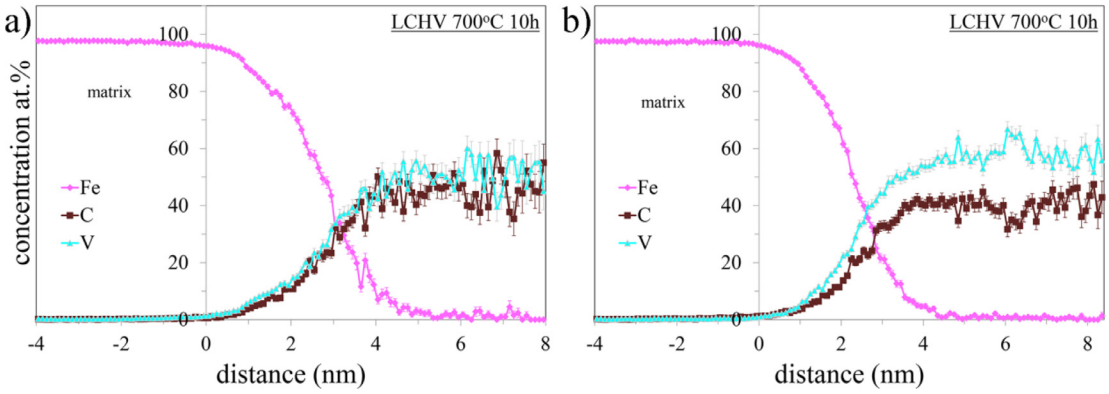

Fig. 10. Proxigrams of two representative precipitates with different stoichiometry in the LCHV steel annealed at 700°C for 10 h. In a), the carbon-to-metal ratio is closer to the stoichiometric ratio than in b).

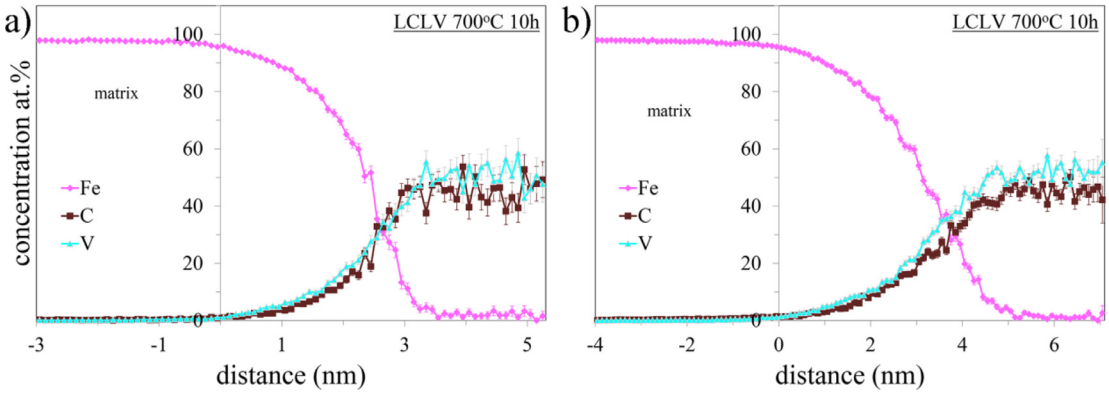

Fig. 11. Representative proximity diagrams of two precipitates differing in stoichiometry in the LCLV steel annealed at 700°C for 10 h. In a), the carbon-to-metal ratio is closer to the stoichiometric ratio than in b).

sake of simplicity. Precipitates with a small and comparable fraction of iron in the core and with different substoichiometric ratios are found in all steels.

The two precipitates in Figs. 10a and 10b are from two different APT tips extracted from the same sample area of the LCHV steel annealed at 700 °C. Fig. 10a shows the radially averaged 1D composition profile of a precipitate in which the carbon-to-metal ratio is close to the stoichiometric one while Fig. 10b shows the profile of a precipitate in which the carbon-to-metal ratio is much lower that the stoichiometric ratio. Such differences in the stoichiometry of the precipitates are found in all alloys. In both precipitates, iron is detected in the core in a fraction of a few at.% which is consistent with the equilibrium precipitate composition given by ThermoCalc.

A gradual increase of vanadium and carbon along with a decrease of iron concentration from the surface to the precipitate core is observed. However, inconsistencies in the concentration profile of the precipitates' surface are possible as a result of the local magnification effect [38] in APT, which causes misidentification of atoms close to the precipitate/matrix interface.

The proxigrams in Figs. 11a and 11b belong to precipitates in the LCLV steel annealed at 700 °C for 10 h. Like in Figs. 10a and 10b, the precipitates in Fig. 11 are from two different tips but from the same sample area of the LCLV steel. The precipitate in Fig. 11a has a composition closer to stoichiometry and the one in Fig. 11b has a lower carbon-to-metal ratio. APT therefore shows that substoichiometric precipitates are also present in the LCLV steel, in which the presence of substoichiometric precipitates is not obvious from the experimental SANS $(d\Sigma/d\Omega)_{NUC}/(d\Sigma/d\Omega)_{MAG}$ ratio evolution (Figs. 4a and 4b). In these figures, the experimental ratio does not reach the green dashed horizontal line which is the theoretical ratio that the precipitates would have if they were stoichiometric. The experimental $(d\Sigma/d\Omega)_{NUC}/(d\Sigma/d\Omega)_{MAG}$ values in the LCLV steel are lower than the theoretical stoichiometric ratio and this can explained by the presence of iron in the precipitates which reduces the $(d\Sigma/d\Omega)_{NUC}/(d\Sigma/d\Omega)_{MAG}$ ratio.

The APT results confirm qualitatively the presence of a distribution of precipitates with different carbon-to-metal ratios, ranging from 0.75 to 1, in the same alloy treated at the same temperature. A quantitative analysis, which would lead to the determination of the substoichiometric distribution of the precipitates, cannot be performed due to the local nature of the APT measurements which leads to limited statistics, to the directional walk effect [43], which causes inconsistencies in the measured carbon concentration, and to the limited effective spatial resolution of APT for small particles or precipitates [67].

The proxigrams also show that precipitates with a similar size can have different carbon-to-metal stoichiometry. This result suggests that the stoichiometry of a precipitate is not only size dependent but also a function of many other factors such as temperature, precipitate coherency, steel nominal composition, time of nucleation or growth/coarsening rate. Due to all these factors, the overall stoichiometry distribution can slightly vary during annealing. For instance, in the early stages of nucleation, iron-rich clusters coherent to the matrix are formed, which later transform into incoherent precipitates that may have different crystal structure [14,68]. The lattice parameter and consequently the coherency of the precipitates is controlled by the solute elements fractions. During the transition from coherent to incoherent particles, the

precipitate-matrix interfacial energy increases thus a larger fraction of vacancies is necessary for the precipitate stability, causing a slight gradual decrease in the carbon-to-vanadium ratio [14]. This could be an additional reason for a slight change in the precipitate stoichiometry during isothermal holding. Small inhomogeneities in the steel chemical composition or slight temperature deviations between different specimen areas can also affect the precipitate chemical composition.

The in-situ SANS measurements are performed in a sample volume of ~10^{20} nm^3, which is approximately 14 orders of magnitude larger than the typical volume that is normally analysed by APT (~10^6 nm^3), consequently probing a larger number of precipitates and therefore providing better statistics on the chemical composition of the precipitates.

5. Conclusions

Our in-situ SANS investigation of the evolution of the precipitate chemical composition at 650 °C and at 700 °C in three vanadium micro-alloyed steels with different vanadium and carbon contents, provides unique insight into the time evolution of the precipitate chemical composition and opens up new possibilities for future investigations.

Our results indicate that precipitation of vanadium carbides takes place according to the following schemes. The precipitates are initially metastable with a high iron concentration and their composition gradually evolves during annealing. The initial high iron concentration in the precipitates can be explained by the ability of iron to reduce the precipitate-matrix misfit and reduce the activation energy for precipitate nucleation. The iron content in the precipitates depends on the steel composition, the annealing temperature, the precipitate size and the annealing time. The fraction of iron in the precipitate is gradually decreasing during annealing, being substituted by vanadium and leading to the formation of the vanadium carbide phase. The precipitates are sub-stoichiometric, i.e., the carbon-to-metal ratio in the precipitates is smaller than 1, possibly because the presence of carbon vacancies in their lattice can increase their stability. Addition of vanadium to the steel nominal composition leads to precipitates that are richer in vanadium and with less iron during the entire precipitation process, in case we assume that the carbon to metal ratio is given by ThermoCalc, i.e. smaller carbon to metal ratio for the alloys with more vanadium.

Faster changes in the precipitate chemical composition are observed at 700 °C in all steels because of the faster diffusion of vanadium at 700 °C than at 650 °C. At the same temperature, at 650 °C or 700 °C, an increase of both vanadium and carbon overall content accelerates the changes in the precipitate chemical composition during annealing as a result of a higher driving force for precipitation.

By in-situ SANS, the chemical composition evolution of the precipitates can be calculated in any steel irrespective of the precipitates shape and size distribution. Complementary APT measurements prove the presence of precipitates with a distribution of carbon-to-metal ratios, ranging from 0.75 to 1, after 10 h at 650 or 700 °C in all steels.

Declaration of Competing Interest

The authors declare that they have no known competing financial interests or personal relationships that could have appeared to influence the work reported in this paper.

Acknowledgements

This work was supported by the Materials innovation institute M2i (www.m2i.nl), project S41.5.14548, in the framework of the M2i Partnership Program, and the Technology Foundation TTW (www.stw.nl), which is part of the Netherlands Organization for Scientific Research (www.nwo.nl). The authors greatly acknowledge the use of the Larmor beamline at ISIS (experiment number RB1869024 [69]) and the Nederlandse Organisatie voor Wetenschappelijk Onderzoek Groot grant no. LARMOR 721.012.102. The authors would like to thank Tata Steel in Europe for providing the materials as hot-rolled plates.

Supplementary materials

Supplementary material associated with this article can be found, in the online version, at doi:10.1016/j.actamat.2020.09.083.

References

[1] European Commission, in: A resource-efficient Europe – Flagship initiative under the Europe 2020 strategy, COM, 2011, p. 21.
[2] K. Seto, Y. Funakawa, and S. Kaneko, Hot rolled high strength steels for suspension and chassis parts “NanoHiten”and “BHT”steel, JFE Technical Report, No. 10, (2007).
[3] A. Rijkenberg, A. Blowey, P. Bellina, C. Wooffindin, Advanced high stretch-flange formability steels for chassis & suspension applications, in: Proceedings of the 4th International Conference on Steels in Cars and Trucks (SCT2014), Braunschweig (Germany), 2014, p. 426.
[4] Y. Funakawa, T. Shiozaki, K. Tomita, T. Yamamoto, E. Maeda, Development of high strength hot-rolled sheet steel consisting of ferrite and nanometer-sized carbides, ISIJ Int 44 (11) (2004) 1945–1951.
[5] T.N. Baker, Microalloyed steels, Ironmak, Steelmak 43 (4) (2016) 264–307.
[6] WO2013167572 (A1), “Automotive Chassis Part Made from High Strength Formable Hot Rolled Steel Sheet”, Tata Steel.
[7] WO2014122215 (A1), A High-Strength Hot-Rolled Steel Strip Or Sheet With Excellent Formability and Fatigue Performance and a Method of Manufacturing Said Steel Strip Or Sheet, Tata Steel.
[8] EP1338665 (A1), High Tensile Hot Rolled Steel Sheet and Method For Production Thereof, JFE Steel Corporation.
[9] R. Lagneborg, T. Siwecki, S. Zajac, B. Hutchinson, The role of vanadium in microalloyed steels, Scand. J. Metall 28 (5) (1999) 186–241.
[10] M.-.Y. Chen, M. Goune, M. Verdier, Y. Brechet, J.-.R. Yang, Interphase precipitation in vanadium-alloyed steels: strengthening contribution and morphological variability with austenite to ferrite transformation, Acta Mater 64 (2014) 78–92.
[11] G. Miyamoto, R. Hori, B. Poorganji, T. Furuhara, Interphase precipitation of VC and resultant hardening in V-added medium carbon steels, ISIJ Int 51 (10) (2011) 1733–1739.
[12] Y.-J. Zhang, G. Miyamoto, K. Shinbo, T. Furuhara, T. Ohmura, T. Suzuki, K. Tsuzaki, Effects of transformation temperature on VC interphase precipitation and resultant hardness in low-carbon steels, Acta Mater 84 (2015) 375–384.
[13] Y.Q. Wang, S.J. Clark, V. Janik, R.K. Heenan, D.A. Venero, K. Yan, D.G. Mc Cartney, S. Sridhar, P.D. Lee, Investigating nano-precipitation in a V-containing HSLA steel using small angle neutron scattering, Acta Mater 145 (2018) 84–96.
[14] J. Wang, M. Weyland, I. Bikmukhametov, M.K. Miller, P.D. Hodgson, I. Timokhina, Transformation from cluster to nano-precipitate in microalloyed ferritic steel, Scr Mater 160 (2019) 53–57.
[15] F. Danoix, E. Bémont, P. Maugis, D. Blavette, I. Atom Probe Tomography, Early Stages of Precipitation of NbC and NbN in Ferritic Steels, Advanced Engineering Materials 8 (12) (2006) 1202–1205.
[16] R.P. Kolli, D.N. Seidman, Co-Precipitated and Collocated Carbides and Cu-Rich Precipitates in a Fe–Cu Steel Characterized by Atom-Probe Tomography, Microsc. Microanal 20 (2014) 1727–1739.
[17] L. Wu, T. Yao, Y. Wang, J. Zhang, F. Xiao, B. Liao, Understanding the mechanical properties of vanadium carbides: Nano-indentation measurement and first-principles calculations, Journal of Alloys and Compounds 548 (2013) 60–64.
[18] W. Xing, F. Meng, R. Yu, A new type of vanadium carbide V_5C_3 and its hardening by tuning Fermi energy, Scientific Reports 6 (2016) 21794.
[19] X. Chong, Y. Jiang, R. Zhoua, J. Feng, Electronic structures mechanical and thermal properties of V–C binary compounds, RSC Adv 4 (2014) 44959–44971.
[20] E. Nembach, Precipitation hardening caused by a difference in shear modulus between particle and matrix, Phys. Stat. Sol. (a) 78 (1984) 571–581.
[21] P. Gong, X.G. Liu, A. Rijkenberg, W.M. Rainforth, The effect of molybdenum on interphase precipitation and microstructures in microalloyed steels containing titanium and vanadium, Acta Mater 161 (2018) 374–387.

[22] Y.-J. Zhang, G. Miyamoto, K. Shinbo, T. Furuhara, Quantitative measurements of phase equilibria at migrating α/γ interface and dispersion of VC interphase precipitates: evaluation of driving force for interphase precipitation, Acta Mater 128 (2017) 166–175.
[23] T.N. Baker, Processes, microstructure and properties of vanadium microalloyed steels, Materials Science and Technology 25 (9) (2009) 1083–1107.
[24] Y. Oba, S. Koppoju, M. Ohnuma, T. Murakami, H. Hatano, K. Sasakawa, A. Kitahara, J. Suzuki, Quantitative analysis of precipitate in vanadium-microalloyed medium carbon steels using small-angle X-ray and neutron scattering methods, ISIJ Int 51 (11) (2011) 1852–1858.
[25] T. Epicier, D. Acevedo, M. Perez, Crystallographic structure of vanadium carbide precipitates in a model Fe-C-V steel, Philos. Mag 88 (1) (2007) 31–45.
[26] C. Ioannidou, Z. Arechabaleta, A. Navarro-López, A. Rijkenberg, R.M. Dalgliesh, S. Kölling, V. Bliznuk, C. Pappas, J. Sietsma, A.A. van Well, S.E. Offerman, Interaction of precipitation with austenite-to-ferrite phase transformation in vanadium micro-alloyed steels, Acta Mater 181 (2019) 10–24.
[27] S. Dhara, R.K.W. Marceau, K. Wood, T. Dorina, I.B. Timokhina, P.D. Hodgson, Precipitation and clustering in a Ti-Mo steel investigated using atom probe tomography and small-angle neutron scattering, Mat. Sci. Eng. A 718 (2018) 74–86.
[28] S. Dhara, R.K.W. Marceau, K. Wood b, T. Dorin, I.B. Timokhina, P.D. Hodgson, Atom probe tomography data analysis procedure for precipitate and cluster identification in a Ti-Mo steel, Data in Brief 18 (2018) 968–982.
[29] S. Jiang, H. Wang, Y. Wu, X. Liu, H. Chen, M. Yao, B. Gault, D. Ponge, D. Raabe, A. Hirata, M. Chen, Y. Wang, Z. Lu, Ultrastrong steel via minimal lattice misfit and high-density nanoprecipitation, Nature 544 (2017) 460–464.
[30] X. Zhang, C. Ioannidou, G.H. ten Brink, A. Navarro-López, J. Wormann, J. Campaniello, R.M. Dalgliesh, A.A. van Well, S.E. Offerman, W. Kranendonk, B.J. Kooi, Microstructure, precipitate and property evolution in cold-rolled Ti-V high strength low alloy steel, Materials and Design 192 (2020) 108720.
[31] H.-W. Yen, P.-Y. Chen, C.-Y. Hunag, J.-R. Yang, Interphase precipitation of nanometer-sized carbides in a titanium-molybdenum-bearing low-carbon steel, Acta Mater 59 (2011) 6264–6274.
[32] C. Ioannidou, Z. Arechabaleta, A. Rijkenberg, R.M. Dalgliesh, A.A . van Well, S.E Offerman, VC-precipitation kinetics studied by small-angle neutron scattering in nano-steels, Mater. Sci. Forum 941 (2018) 236–244.
[33] M. Nöhrer, S. Zamberger, S. Primig, H. Leitner, Atom probe study of vanadium interphase precipitates and randomly distributed vanadium precipitates in ferrite, Micron 54-55 (2013) 57–64.
[34] Y.S. Shanmugam, M. Tanniru, R.D.K. Misra, D. Panda, S. Jansto, Microalloyed V–Nb–Ti and v steels part 2, precipitation behavior during processing of structural beams, Mater. Sci. Tech 21 (2) (2005) 165–177.
[35] G. Miyamoto, R. Hori, B. Poorganji, T. Furuhara, Crystallographic analysis of proeutectoid ferrite/austenite interface and interphase precipitation of vanadium carbide in medium-carbon steel, Metall. Mater. Trans. A 44A (2013) 3436–3443.
[36] Y. Ishiguro, K. Sato, Determination of Non-Stoichiometric Composition of Complex Carbon-Nitrides in Steel by Measuring Plasmon Energy, Materials Transactions, JIM 37 (4) (1996) 643–649.
[37] C.E.I.C. Öhlund, J. Weidow, M. Thuvander, S.E. Offerman, Effect of Ti on evolution of microstructure and hardness of martensitic fe–c–mn steel during tempering, ISIJ Intern 54 (12) (2014) 2890–2899.
[38] Y.-J. Zhang, G. Miyamoto, K. Shinbob, T. Furuhara, Effects of α/γ orientation relationship on VC interphase precipitation in low-carbon steels, Scr Mater 69 (2013) 17–20.
[39] E.A. Marquis, J.M. Hyde, Applications of atom-probe tomography to the characterization of solute behaviours, Mater. Sci. Eng. R 69 (2010) 37–62.
[40] F.L. Alcântara, R. Barbosa, M.A. Cunha, Study of aluminum nitride precipitation in Fe- 3%Si steel, Mater. Res 16 (2013) 1039–1044.
[41] J. Lu, J.B. Wiskel, O. Omotoso, H. Henein, D.G. Ivey, Matrix dissolution techniques applied to extract and quantify precipitates from a microalloyed steel, Metall. Mater. Trans. A Phys. Metall. Mater. Sci 42 (2011) 1767–1784.
[42] A.L. Rivas, E. Vidal, D.K. Matlock, J.G. Speer, Electrochemical extraction of microalloy carbides in Nb-steel, Rev. Metal 44 (2008) 447–456.
[43] B. Gault, F. Danoix, K. Hoummada, D. Mangelinck, H. Leitner, Impact of directional walk on atom probe microanalysis, Ultramicroscopy 113 (2012) 182–191.
[44] F. Perrard, A. Deschamps, F. Bley, P. Donnadieua, P. Maugis, A small-angle neutron scattering study of fine-scale NbC precipitation kinetics in the a-Fe–Nb–C system, J. Appl. Cryst. 39 (2006) 473–482.
[45] N.H. van Dijk, S.E. Offerman, W.G. Bouwman, M.Th. Rekveldt, J. Sietsma, S. van der Zwaag, A. Bodin, R.K. Heenan, High Temperature SANS experiments on Nb(C,N) and MnS precipitates in HSLA steel, Metall. Mater. Trans. A 33 (2002) 1883–1891.
[46] , Wiedenmann, Small angle scattering investigations of magnetic nanostructures, in: T. Chatterji (Ed.), Neutron Scattering from Magnetic Materials, Elsevier, 2006, pp. 473–519.
[47] T.H. Simma, L. Sunb, D.R. Galvina, E.P. Gilbertc, D.A. Venerof, Y. Lia, T.L. Martine, P.A.J. Bagote, M.P. Moodye, P. Hilld, H.K.D.H. Bhadeshia, S. Biroscaa, M.J. Rawsond, K.M. Perkins, A SANS and APT study of precipitate evolution and strengthening in a maraging steel, Mater. Sci. Eng. A 702 (2017) 414–424.
[48] B.S. Seong, E. Shin, S. Choi, Y. Choi, Y.S. Han, K.H. Lee, Y. Tomota, Quantitative analysis of fine nano-sized precipitates in low-carbon steels by small angle neutron scattering, Appl. Phys. A 99 (2010) 613–620.
[49] J.O. Andersson, T. Helander, L. Höglund, P.F. Shi, B. Sundman, Thermo-Calc and Dictra, Comp. Tools Mater. Sci. Calphad 26 (2002) 273–312.
[50] A. Navarro-López, C. Ioannidou, E. van der Wal, Z. Arechabaleta, R. van der Oever, M. Verleg, R. Dalgliesh, J. Sykora, F. Akeroyd, J. Sietsma, C. Pappas, A. A. van Well, S. E. Offerman, Furnace for In-situ and Simultaneous Studies of Nano-Precipitates and Phase Transformations in Steels with by SANS and Neutron Diffraction, submitted to Review of Scientific Instruments.
[51] O. Arnold, J.C. Bilheux, J.M. Borreguero, A. Buts, S.I. Campbell, L. Chapon, M. Doucet, N. Draper, R. Ferraz Leal, M.A. Gigg, V.E. Lynch, A. Markvardsen, D.J. Mikkelson, R.L. Mikkelson, R. Miller, K. Palmen, P. Parker, G. Passos, T.G. Perring, P.F. Peterson, S. Renc, M.A. Reuter, A.T. Savici, J.W. Taylor, R.J. Taylor, R. Tolchenov, W. Zhou, J. Zikovsky, Mantid-Data analysis and visualization package for neutron scattering and μsr experiments, Nuc. Inst. Meth. Phys. Res. A 764 (2014) 156–166.
[52] D.J. Larson, D.T. Foord, A.K. Petford-Long, T.C. Anthony, I.M. Rozdilsky, A. Cerezo, G.W.D. Smith, Focused ion-beam milling for field-ion specimen preparation: preliminary investigations, Ultramicroscopy 75 (1998) 147–159.
[53] M. Thuvander, J. Weidow, J. Angseryd, L.K. Falk, M. Sonestedt, K. Stiller, H.O. Andrén, Quantitative atom probe analysis of carbides, Ultramicroscopy 111 (2011) 604–608.
[54] R. Córdoba, N. Sharma, S. Kölling, P.M. Koenraad, B. Koopmans, High-purity 3D nano-objects grown by focused-electron-beam induced deposition, Nanotechnology 27 (2016) 355301.
[55] P. Bas, A. Bostel, B. Deconihout, D. Blavette, A general protocol for the reconstruction of 3D atom probe data, Applied Surface Science 87/88 (1995) 298–304.
[56] T. Narayanan, Synchrotron small-angle X-Ray scattering, in: R. Borsali, R. Pecora (Eds.), Soft-Matter Characterization, Springer, 2008, pp. 899–948.
[57] L. A. Feigin, Structure Analysis by Small-Angle X-ray and Neutron Scattering, New York, 1987.
[58] E.K. Storms, C.P. Kempter, Thermal Expansion of Some Vanadium Carbides, Chem. Phys 42 (1965) 2043–2045.
[59] M. Onink, C.M. Brakman, F.D. Tichelaar, E.J. Mittemeijer, S. van der Zwaag, J.H. Root, N.B. Konyer, The lattice parameters of austenite and ferrite in Fe-C alloys as functions of carbon concentration and temperature, Scr Metala et Mater 29 (8) (1993) 1011–1016.
[60] Z. Sun, R. Ahuja, J.E. Lowther, Mechanical properties of vanadium carbide and a ternary vanadium tungsten carbide, Solid State Communications 150 (2010) 697–700.
[61] V.F. Sears, Neutron scattering lengths and cross sections, Neutron News 3 (3) (1992) 26–37.
[62] A.S. Arrott, B. Heinrich, Application of magnetization measurements in iron to high temperature thermometry, Journal of Applied Physics 52 (1981) 2113–2115.
[63] Y.-J. Zhang, G. Miyamoto, K. Shinbo, T. Furuhara, Weak influence of ferrite growth rate and strong influence of driving force on dispersion of VC interphase precipitation in low carbon steels, Acta Materialia 186 (2020) 533–544.
[64] H. Sharma, J. Sietsma, S.E. Offerman, Preferential Nucleation during Polymorphic Transformations, Scientific Reports 6 (2016) 30860.
[65] S.E. Offerman, N.H. van Dijk, J. Sietsma, S. van der Zwaag, E.M. Lauridsen, L. Margulies, S. Grigull, H.F. Poulsen, Reply to the discussion by Aaronson et al. to "Grain nucleation and growth during phase transformations" by S.E. Offerman et al., Science, 298, 1003 (November 1, 2002), Scr Mater 51 (2004) 937–941.
[66] O.C. Hellman, J.A. Vandenbroucke, J. Rusing, D. Isheim, D.N. Seidman, Analysis of three-dimensional atom-probe data by the proximity histogram, Microsc. Microanal 6 (2000) 437–444.
[67] F. De Geusera, B. Gault, Metrology of small particles and solute clusters by atom probe tomography, Acta Mater 188 (2020) 406–415.
[68] H. Sawada, S. Taniguchi, K. Kawakami, T. Ozaki, Transition of the Interface between Iron and Carbide Precipitate From Coherent to Semi-Coherent, Metals 7 (2017) 277.
[69] S.E. Offerman, E. van der Wal, A.A. van Well, A. Navarro-López, C. Ioannidou, R.M. Dalgliesh, In-situ and simultaneous SANS and ND to study the precipitation and phase transformation kinetics in V-containing Nano-steels, STFC ISIS Neutron and Muon Source (2019), doi:10.5286/ISIS.E.RB1869024.